Electrical and Elastic Properties of Individual Single-Layer Nb$_4$C$_3$T$_x$ MXene Flakes

Alexey Lipatov,[1] Mohamed Alhabeb,[2,3] Haidong Lu,[4] Shuangshuang Zhao,[5] Michael J. Loes,[1] Nataliia S. Vorobeva,[1] Yohan Dall'Agnese,[5,†] Yu Gao,[5] Alexei Gruverman,[4,6] Yury Gogotsi,[2,3,5,*] Alexander Sinitskii[1,6,*]

[1] Department of Chemistry, University of Nebraska-Lincoln, Lincoln, NE 68588, USA

[2] A.J. Drexel Nanomaterials Institute, Drexel University, Philadelphia, PA 19104, USA

[3] Department of Materials Science & Engineering, Drexel University, Philadelphia, PA 19104, USA

[4] Department of Physics and Astronomy, University of Nebraska-Lincoln, Lincoln, NE 68588, USA

[5] Key Laboratory of Physics and Technology for Advanced Batteries (Ministry of Education), College of Physics, Jilin University, Changchun 130012, PR China

[6] Center for Materials and Nanoscience, University of Nebraska-Lincoln, Lincoln, NE 68588, USA

* Corresponding authors: sinitskii@unl.edu, gogotsi@drexel.edu

† Present address: Institute for Materials Discovery, University College London, London WC1E 7JE, UK

Abstract

2D carbides and nitrides (MXenes) are widely recognized for their exceptional promise for numerous applications. However, physical property measurements of their individual monolayers remain very limited despite their importance for revealing the intrinsic physical properties of MXenes. The first mechanical and electrical measurements of individual single-layer flakes of Nb$_4$C$_3$T$_x$ MXene, which are prepared via an improved synthetic method are

reported. Characterization of field-effect transistor devices based on individual single-layer $Nb_4C_3T_x$ flakes shows an electrical conductivity of 1024 ± 165 S cm^{-1}, which is two orders of magnitude higher than the previously reported values for bulk $Nb_4C_3T_x$ assemblies, and an electron mobility of 0.41 ± 0.27 cm^2 V^{-1} s^{-1}. Atomic force microscopy nanoindentation measurements of monolayer $Nb_4C_3T_x$ membranes yield an effective Young's modulus of 386 ± 13 GPa, assuming a membrane thickness of 1.26 nm. This is the highest value reported for nanoindentation measurements of solution-processable 2D materials, revealing the potential of $Nb_4C_3T_x$ as a primary component for various mechanical applications. Finally, the agreement between the mechanical properties of 2D $Nb_4C_3T_x$ MXene and cubic NbC suggests that the extensive experimental data on bulk carbides could be useful for identifying new MXenes with improved functional characteristics.

Introduction

MXenes are a large class of 2D transition metal carbides (TMCs), nitrides, and carbonitrides that show a great promise for a variety of electronic,[1-4] energy storage,[5,6] and biomedical applications.[7-9] MXenes have a general formula of $M_{n+1}X_nT_x$, where M is a transition metal (Ti, Zr, Nb, V, Ta, Cr, etc.), X is carbon or nitrogen, $n = 1, 2, 3$, or 4, and T_x represents the surface functionalization of 2D sheets by various moieties, such as fluorine, oxygen, and hydroxyl groups.[6,10] The surface functional groups are the result of the chemical process that is used for the synthesis of MXenes, which is based on selective solution etching of layers of an "A" element (typically Al or Si) from ternary TMCs and nitrides, known as MAX phases.[6,10] Over the last few years, the MXene family has been rapidly growing, as more than 30 different stoichiometric structures, such as $Ti_3C_2T_x$, Ti_2CT_x, Nb_2CT_x, $Nb_4C_3T_x$, V_2CT_x, and $Mo_2TiC_2T_x$, were experimentally demonstrated and many others were theoretically predicted.[6]

One of the important advantages of MXenes is that they can be synthesized in large quantities and used for bulk applications in a form of, for example, large-area conductive films,[1-3] battery and supercapacitor electrodes, binders and current collectors of energy storage devices, antennas, and electromagnetic interference shields.[5,6,11] As a result, MXenes have been typically studied in various macroscopic assemblies of 2D flakes processed as films or 3D scaffolds or composites.[12] Physical measurements of such assemblies naturally reveal an interplay of intrinsic MXenes' properties and various interfacial phenomena between 2D flakes.[13] The intrinsic properties of MXenes could be determined in measurements of

individual monolayer flakes that, however, have been very scarce so far and limited only to $Ti_3C_2T_x$,[14-16] the most popular MXene material to date,[17] and Ti_3CNT_x.[13] The measurements performed on individual flakes of $Ti_3C_2T_x$ revealed its remarkable electronic[14,15] and mechanical properties.[16] Individual monolayer $Ti_3C_2T_x$ flakes were shown to have a high electrical conductivity of about 4600 S cm^{-1},[14] and their nanoindentation measurements revealed the effective Young's modulus of 0.33 ± 0.03 TPa, which is the highest among the values previously reported in similar nanoindentation experiments for other solution-processed 2D materials, including graphene oxide (GO) and reduced graphene oxide (rGO).[16]

The remarkable elastic characteristics of $Ti_3C_2T_x$ were not unexpected, considering that TMCs are known for their exceptional bulk mechanical properties.[18] Thus, in search for 2D MXenes with even higher Young's moduli, it is reasonable to consider their bulk TMC counterparts, which have been studied for decades. For example, a nonfunctionalized Ti_3C_2 sheet with a hexagonal structure could be viewed as a (111) slab of a cubic TiC crystal, for which the Young's modulus was measured to be about 400 GPa.[19] We considered other experimentally demonstrated MXenes[6] and found that a sheet of $Nb_4C_3T_x$[20] without surface functionalities could be viewed as a (111) slab of a cubic NbC crystal, which is illustrated by Figure 1. The Young's modulus of bulk NbC was previously reported to be 452–488 GPa,[21,22] which are higher values than for cubic TiC.
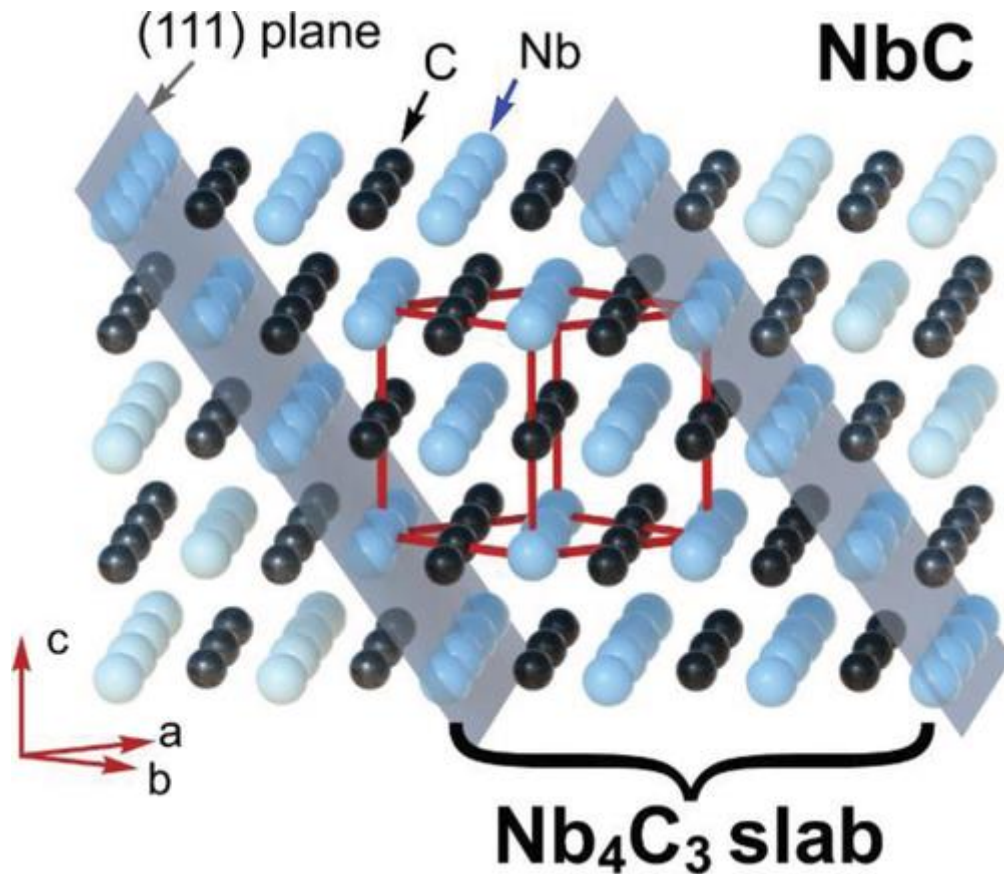
Figure 1. A scheme showing an Nb_4C_3 sheet as a part of the NbC cubic structure. The unit cell of NbC is shown in red. The scheme demonstrates the structural relationship between bulk NbC crystals and $Nb_4C_3T_x$ MXene, and the fact that known properties of bulk transition metal carbides could be used for estimating properties of related MXene materials.

Motivated by this preliminary assessment, we performed mechanical and electrical characterization of individual single-layer flakes of $Nb_4C_3T_x$ MXene (Figure 2a), which have not been previously reported in literature. We found the effective Young's modulus for $Nb_4C_3T_x$ monolayers to be 386 ± 14 GPa, which indeed is higher than for $Ti_3C_2T_x$ MXene[16] and sets up a new record for elastic properties of solution-processable 2D materials determined in nanoindentation experiments. These results establish $Nb_4C_3T_x$ as a promising material for a variety of mechanical applications, including structural composites, fibers, textiles, protective coatings, nanoresonators, and membranes. The electrical conductivity of individual $Nb_4C_3T_x$ monolayers was measured at 1024 ± 165 S cm^{-1}, which is two orders of magnitude higher than the previously reported values for $Nb_4C_3T_x$ macroscopic thin films,[20] again demonstrating the importance of single-flake measurements for revealing the intrinsic physical properties of MXene materials.
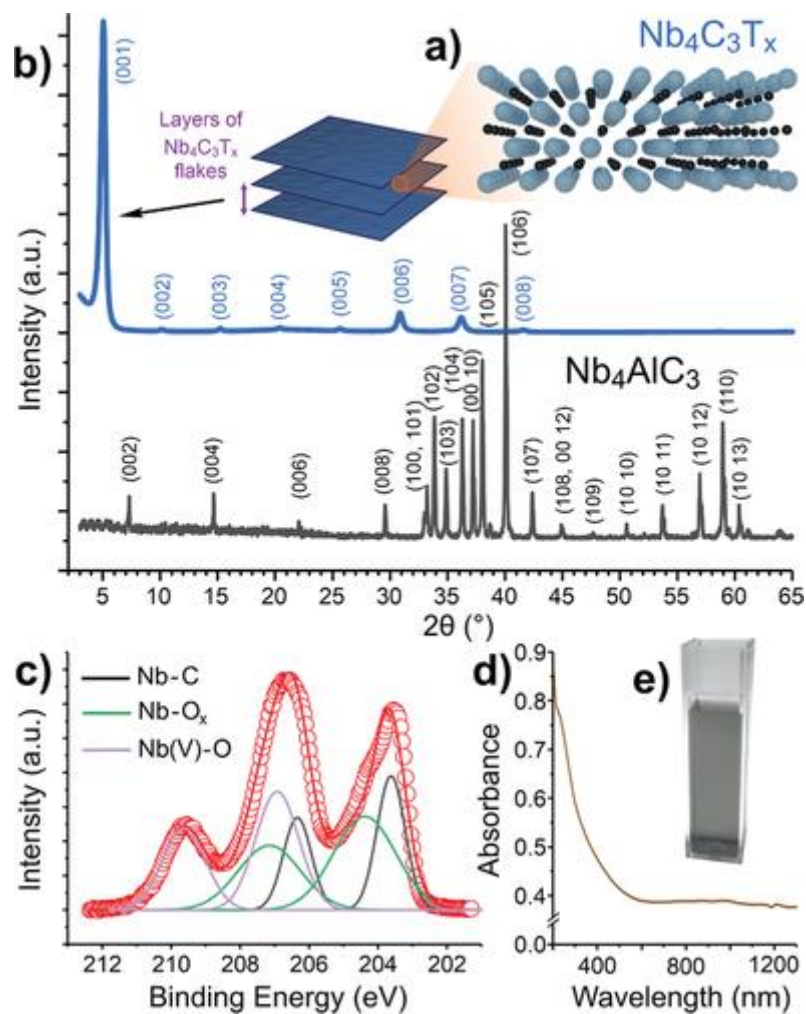
Figure 2. Characterization of $Nb_4C_3T_x$ flakes. a) Crystal structure of $Nb_4C_3T_x$ MXene. Nb—blue spheres, C—black spheres, the surface functional groups (T_x) are omitted. b) XRD spectra of the precursor Nb_4AlC_3 MAX phase (black) and the $Nb_4C_3T_x$ powder (blue). c) XPS Nb3d spectrum of $Nb_4C_3T_x$. The circles show the experimental data, while the solid curves show their fitting. d) UV–vis–NIR absorption spectrum of $Nb_4C_3T_x$ aqueous suspension. e) Photograph of an $Nb_4C_3T_x$ aqueous suspension in a cuvette.

Single-flake studies generally require uniform MXene flakes with sizes exceeding at least 1 µm to fabricate field-effect transistors (FETs) and membranes for electrical[13,14] and mechanical measurements,[16] respectively. In this article, we present an improved method for the synthesis of $Nb_4C_3T_x$ to produce well-exfoliated flakes of sufficient size and quality for electrical and mechanical characterization.

2 Synthesis and Materials Characterization of $Nb_4C_3T_x$

For MXene synthesis, 0.4 g of Nb_4AlC_3 MAX phase[20] was etched in 30 mL of 50% HF solution with stirring for 140 h at room temperature (20–25 °C). The sample was washed several times by centrifugation (5000 rpm, 6 min each cycle) with deionized (DI) water until the pH became close to 7 to obtain the $Nb_4C_3T_x$ powder. Delamination was performed by adding 1 mL of 25% tetramethylammonium hydroxide (TMAOH) and 9 mL of DI water, shaking for 15 min, and then centrifuging. Centrifugation (3500 rpm, 15 min) was repeated until a colloidal solution was obtained.

Powder X-ray diffraction (XRD) provides a tool to evaluate the effectiveness of MXene synthesis.[14] When the conversion of a MAX phase precursor to MXene is complete, the produced flakes are large, uniform in thickness, and align well in a film, and the XRD pattern of a dried MXene film demonstrates an extended series of (00l) reflections. Figure 2b shows the XRD spectrum of $Nb_4C_3T_x$ MXene that was produced in this study. The spectrum demonstrates equidistantly spaced (00l) peaks ranging from (001) to (008), indicating a layered structure of stacked MXene flakes. Note that since MXene films contain randomly assembled 2D flakes with one Nb_4C_3 layer per unit cell, unlike two such layers in the Nb_4AlC_3 unit cell, we indexed planes starting from (001). The XRD spectrum of the precursor Nb_4AlC_3 MAX phase is shown for comparison. No peaks of the precursor material are observed in the XRD spectrum of $Nb_4C_3T_x$, confirming the complete conversion of the MAX phase to MXene. The interplanar distance extracted from the $Nb_4C_3T_x$ XRD spectrum is about 1.73 nm, which is slightly larger than the values previously reported based on powder diffraction data ($\approx$1.5 nm)[20] and transmission electron microscopy (TEM) imaging ($\approx$1.54 nm[23] and $\approx$1.43 nm[20]). It should be noted that the interplanar distances extracted from the XRD data are affected by the presence of intercalated species between the MXene sheets (water and residual TMAOH), which in turn depend on the sample preparation procedure and measurement conditions, such as relative humidity and temperature. For example, for bulk assemblies of rGO sheets, which share many similarities with MXenes because of their 2D nature and surface functionalization with oxygen-containing functionalities forming strong hydrogen bonds with water molecules, the interplanar distance was shown to vary in a very wide range from 0.6 to 1.2 nm depending on the humidity.[24] The intrinsic thickness of the $Nb_4C_3T_x$ flakes was estimated to be about 1.26 nm, which was calculated by combination of the crystallographic height of bare Nb_4C_3 (0.76 nm) and the height estimate for terminal groups in $Ti_3C_2T_x$ (0.50 nm).[25] This thickness value was used for further analysis of electronic and elastic properties of $Nb_4C_3T_x$.

The results of X-ray photoelectron spectroscopy (XPS) characterization of drop-cast MXene films were consistent with the previously published data for $Nb_4C_3T_x$.[23] A high-resolution XPS Nb$3d$ spectrum presented in Figure 2c could be fitted with three pairs of components:[26] 1) Nb-C belonging to pure MXene phase (203.6 eV for Nb3$d_{5/2}$ and 206.3 eV for Nb3$d_{3/2}$); 2) MXene's Nb bound to the surface functional groups, which could be represented as $NbC_xO_yF_z$ (204.4 eV for Nb3$d_{5/2}$ and 207.2 eV for Nb3$d_{3/2}$); 3) oxidized Nb (207.0 eV for Nb3$d_{5/2}$ and 209.7 eV for Nb3$d_{3/2}$). Interestingly, while XPS analysis suggests some degree of oxidation in a bulk MXene material, we did not find any microscopic evidence for oxidation in high-quality $Nb_4C_3T_x$ flakes that were later used for electrical and mechanical characterization. In the atomic force microscopy (AFM) images, the $Nb_4C_3T_x$ flakes looked smooth and uniform, and when we further studied them by TEM, we did not observe previously reported NbO_x nanoparticles[27] and found a very regular Nb arrangement in the atomically resolved images. The results of AFM and TEM characterization of $Nb_4C_3T_x$ flakes are discussed below in detail. Therefore, the XPS results likely suggest some degree of inhomogeneity in bulk $Nb_4C_3T_x$ samples in which some particles could be more oxidized than others.

A UV–vis–near IR (NIR) absorption spectrum of an aqueous suspension of $Nb_4C_3T_x$ shows high and featureless absorption in the visible range of spectrum (Figure 2d), which is consistent with the visual appearance of the sample (Figure 2e). Interestingly, very similar UV–vis–NIR spectra were previously reported for the Nb_2CT_x nanosheets, which were used for photothermal tumor eradication due to their high optical absorption in NIR-I and NIR-II biological transparency windows.[27] The close similarity between the optical spectra of Nb_2CT_x and $Nb_4C_3T_x$ suggests that the latter may also be considered for similar biomedical applications.

An aqueous suspension of $Nb_4C_3T_x$ flakes (Figure 2e) can be conveniently drop-cast onto various substrates, such as TEM grids, Si/SiO$_2$, and polydimethylsiloxane (PDMS), for further characterization. TEM images of $Nb_4C_3T_x$ flakes are shown in Figure 3a–c. A low-magnification TEM image in Figure 3a shows that the flakes are several micrometers large and uniform in color, indicating the complete exfoliation and the absence of contamination during the synthesis and sample preparation. A hexagonal hole that we observed in one of the flakes (Figure 3b) is consistent with the hexagonal structure of Nb_4C_3 MXene and is likely inherited from a precursor MAX phase crystal.[20] A selected area electron diffraction pattern recorded

from the flake shown in Figure 3a exhibits sharp reflections arranged in hexagonal pattern (Figure 3d), confirming the single-crystal nature of the $Nb_4C_3T_x$ flakes produced in this study.
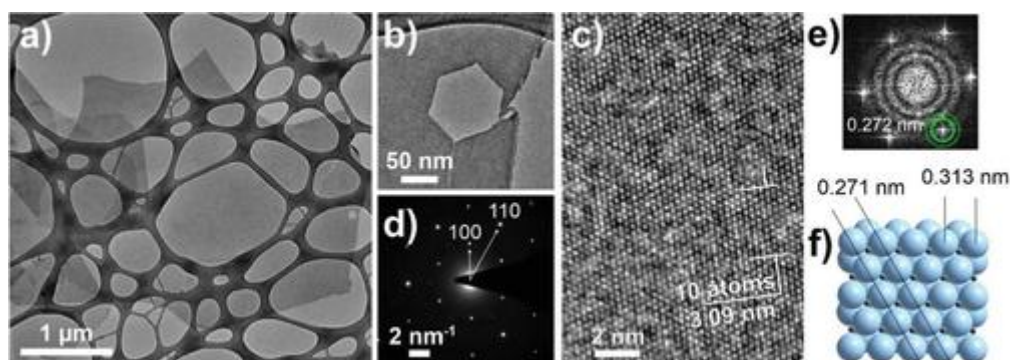

Figure 3. TEM imaging of $Nb_4C_3T_x$ flakes. a–c) TEM images of monolayer $Nb_4C_3T_x$ flakes at different magnifications. d) Selected area electron diffraction pattern of a single-layer $Nb_4C_3T_x$ flake. e) Fourier transform image of the atomic structure shown in panel (c). f) A fragment of the $Nb_4C_3T_x$ crystal structure comprising two layers of Nb atoms (blue spheres) and a layer of carbon atoms (black spheres) together with characteristic distances.

The high quality of the $Nb_4C_3T_x$ flakes was further verified by high-resolution TEM (HRTEM), which revealed the long-range order in the perfect hexagonal arrangement of Nb atoms (Figure 3c). A direct measurement reveals the interatomic Nb–Nb distance of about 0.309 nm (Figure 3c), while the Fourier transform pattern (Figure 3e) of the HRTEM image shows a hexagonal pattern with reflexes corresponding to the 0.272 nm distance between the rows of Nb atoms. Both of these values perfectly agree with the corresponding distances in the theoretical crystal structure of Nb_4C_3 (Figure 3f).

3 Study of the Thickness of $Nb_4C_3T_x$ Flakes

Figure 4 presents the results of the AFM analysis of $Nb_4C_3T_x$ flakes on a Si/SiO_2 substrate. The flakes are several micrometers in size, have smooth and uniform surfaces, and bear no visible signs of degradation. Figure 4a shows a representative AFM image of single-layer (1L) and double-layer (2L) $Nb_4C_3T_x$ flakes. The AFM height profile measured across these flakes shows that the 1L $Nb_4C_3T_x$ flake has a thickness of about 2.7 nm, while the 2L $Nb_4C_3T_x$ flake is thicker by about 1.8 nm (Figure 4b). It is important to recognize that AFM measurements typically overestimate thicknesses of 2D materials due to the presence of surface adsorbates, trapped interfacial molecules, and various instrumental factors.[16,28] In case of the mechanically exfoliated 2D crystals, such as graphene, that are produced in dry conditions, AFM thickness

measurements were shown to be more accurate for few-layer samples, in which the thickness of a top monolayer was measured relative to the height of the layer below.[29,30] In such cases, the inaccuracy in the AFM thickness measurements of the bottom-most monolayers in few-layer 2D crystals was shown to be due to the presence of trapped adsorbate molecules, such as water, under the flakes.[31,32] However, in case of a 2L crystal produced in a liquid environment, such as the 2L MXene flake in Figure 4a, even though its layers originated from the same Nb_4AlC_3 grain, there should be an intercalation of the solvent molecules between the constituent $Nb_4C_3T_x$ monolayers, especially in the view of hydrogen bonding between the water molecules and surface functionalities in $Nb_4C_3T_x$. This conclusion is supported by the AFM image of two 1L $Nb_4C_3T_x$ flakes that overlapped during the deposition on Si/SiO_2 substrate (Figure 4c). The overlap region with the interfacial adsorbates has the same 1.8 nm step height relative to the monolayer regions (Figure 4d) as the height difference between the 2L and 1L $Nb_4C_3T_x$ flakes (Figure 4b). This observation suggests that in both cases, 1.8 nm represents not only the thickness of an $Nb_4C_3T_x$ monolayer, but also the additional thickness of adsorbate molecules. The AFM step height of 1.8 nm is also very close to the interplanar distance (1.73 nm) extracted from the XRD pattern of an $Nb_4C_3T_x$ film (Figure 2b). Given that the theoretical thickness of $Nb_4C_3T_x$ is only 1.26 nm, the multilayer MXene samples measured in this study in ambient conditions likely contained residual TMAOH and water molecules trapped between the layers.
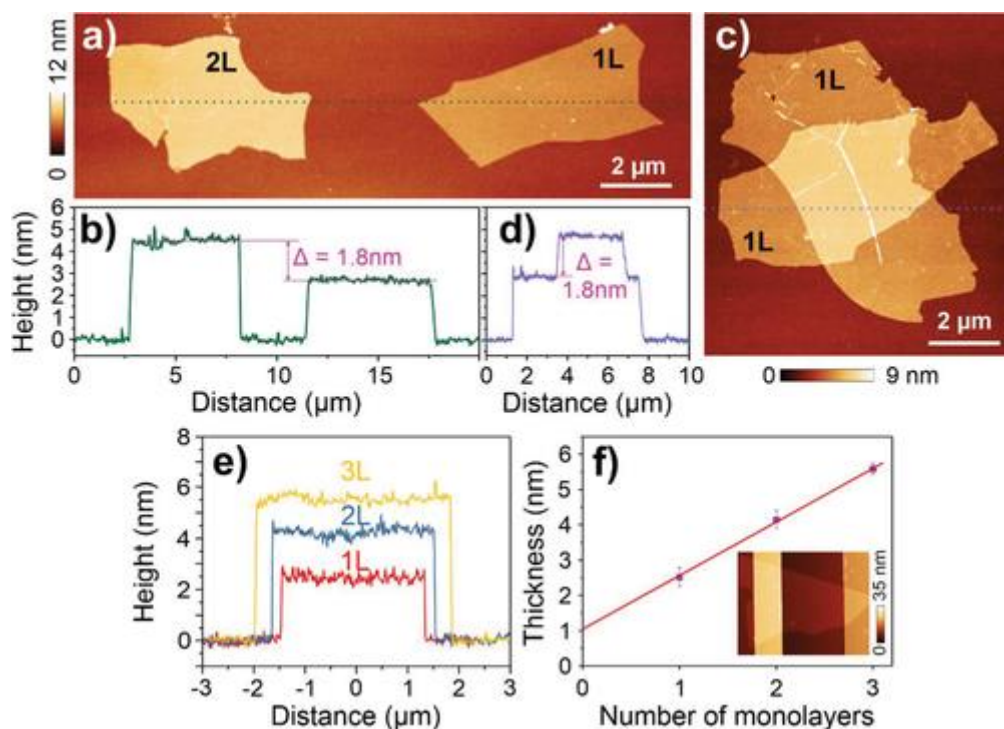
Figure 4. AFM imaging and thickness analysis of $Nb_4C_3T_x$ MXene flakes. a) AFM image of 2L and 1L $Nb_4C_3T_x$ flakes. b) AFM height profile across the 2L and 1L $Nb_4C_3T_x$ flakes measured along the dashed line in panel (a). c) AFM image of two overlapping monolayer $Nb_4C_3T_x$ flakes. d) AFM height profile measured along the dashed line in panel (c). e) Representative AFM cross sections of vacuum-dried MXene flakes containing 1L, 2L and 3L $Nb_4C_3T_x$ flakes. f) The dependence of the averaged thicknesses of several vacuum-dried MXene flakes on the number of $Nb_4C_3T_x$ monolayers. Purple squares are experimental data and red line is a linear fitting. The inset shows AFM image of one of the devices based on a monolayer $Nb_4C_3T_x$ flake, which was vacuum-dried in a probe station at about 10^{-6} Torr. The vertical stripes represent the device electrodes, which where 1.5 µm wide.

The presence of intercalated molecules between the layers of few-layer $Nb_4C_3T_x$ crystals was further confirmed by AFM measurements of MXene flakes on Si/SiO_2 that were vacuum dried for several days at a pressure of about 10^{-6} Torr. Figure 4e shows representative AFM height profiles measured across the vacuum-dried $Nb_4C_3T_x$ flakes with different thicknesses. The 1L $Nb_4C_3T_x$ had a thickness of about 2.5 nm, which is smaller than 2.7 nm measured for the monolayer flakes that were only handled in air (Figure 4a–d) and indicates partial removal of the adsorbate molecules. Likewise, after the vacuum drying, the thickness of 2L $Nb_4C_3T_x$ flakes decreased from about 4.5 nm (Figure 4a–d) to ≈4.1 nm, while trilayer (3L) flakes had a thickness of about 5.8 nm (Figure 4e). A linear fit of the dependence of the AFM thicknesses of several vacuum-dried $Nb_4C_3T_x$ flakes on the number of layers is shown in Figure 4f; each data point represents over 30 height profile measurements. The fit resulted in the thickness of an $Nb_4C_3T_x$ monolayer of 1.5 nm (the slope of the line), which is still larger than the theoretical thickness of 1.26 nm, probably due to the incomplete removal of the intercalated water and TMAOH molecules. The intercept of the fit (≈1.0 nm) likely corresponds to the molecular adsorbates under the flakes. Collectively, the AFM results demonstrated in Figure 4 prove the molecular intercalation between the $Nb_4C_3T_x$ layers and show that the theoretical thickness (1.26 nm) should be used for the analysis of intrinsic mechanical properties of $Nb_4C_3T_x$ monolayers rather than the AFM-measured thickness that is highly dependent on the sample preparation and measurement conditions.

4 Electronic Properties of Individual $Nb_4C_3T_x$ Single-Layer Flakes

For device fabrication, an aqueous suspension of $Nb_4C_3T_x$ flakes (Figure 2e) was spin-coated on a p-type silicon substrate covered with a 300-nm-thick layer of SiO_2. Randomly arranged

individual $Nb_4C_3T_x$ flakes are well visible on this substrate and can be seen in the optical photograph shown in Figure 5a. The majority of the flakes in this image are MXene monolayers, which exhibit a good optical contrast on Si/SiO_2 (300 nm), while thicker flakes are visibly darker. The shape of the flakes can be better seen at a higher magnification in the scanning electron microscopy (SEM) image in Figure 5b. The synthetic procedure disclosed in this work produces uniform $Nb_4C_3T_x$ flakes with lateral dimensions often exceeding 10 µm (Figure S1, Supporting Information). Such large flakes are well suited for device fabrication and characterization of MXene's electrical and mechanical properties. Several two- and four-terminal $Nb_4C_3T_x$ FETs were patterned using electron beam lithography, and Cr/Au contacts were deposited by electron-beam evaporation. The scheme of four-terminal devices fabricated in this study is shown in Figure 5c, demonstrating an $Nb_4C_3T_x$ flake on a 300 nm SiO_2 dielectric layer and a heavily doped p-type Si serving as a gate (G) electrode. The flake bridges drain (D) and source (S) electrodes and is also connected to two voltage probe electrodes (V_1 and V_2). SEM image of a representative four-terminal device with a monolayer MXene channel is shown in Figure 5d; SEM images of several two-terminal devices that do not contain inner voltage probes are provided in Figure S2, Supporting Information.
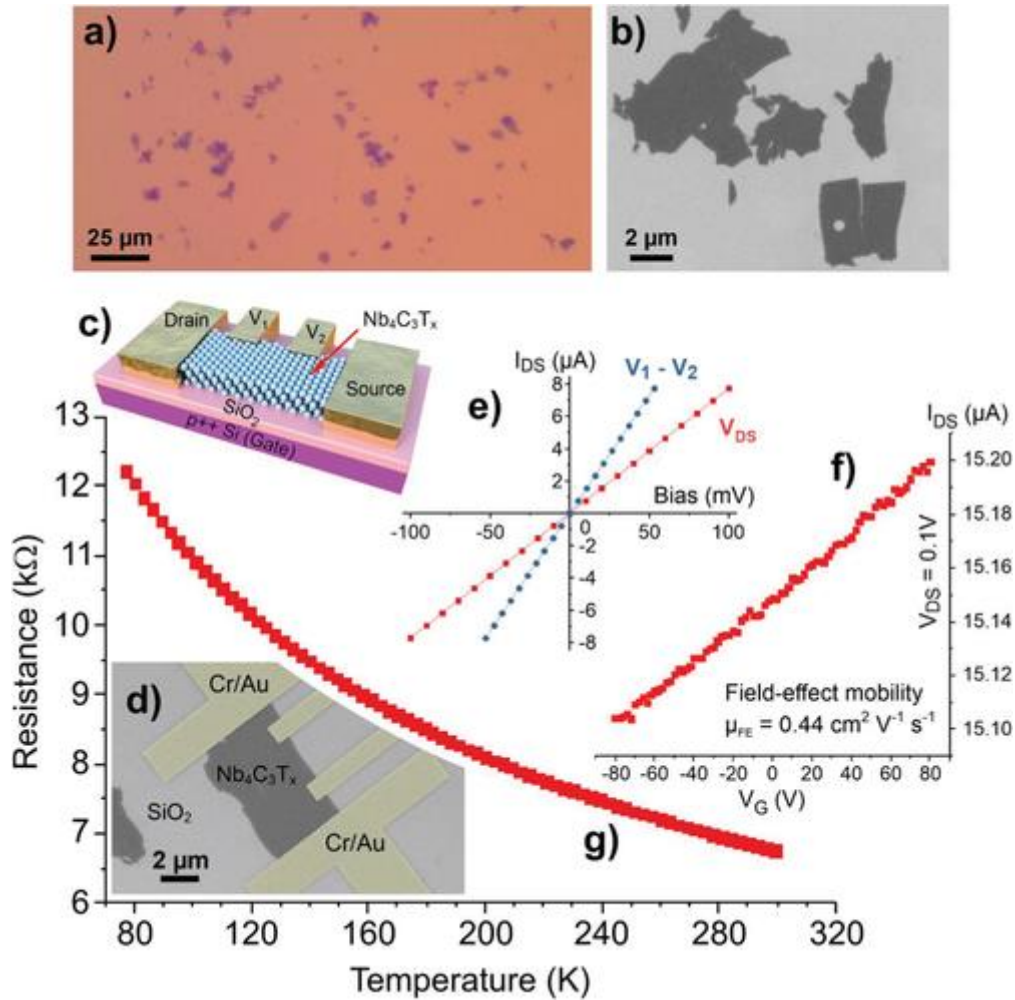
Figure 5. Characterization of electrical properties of $Nb_4C_3T_x$ flakes. a) Optical photograph of $Nb_4C_3T_x$ flakes spin-coated on a Si/SiO_2 substrate. b) SEM image of the same substrate as in panel (a) showing MXene flakes at a higher magnification. c) Scheme of a four-terminal device with $Nb_4C_3T_x$ channel. d) False-colored SEM image of a four-terminal device based on a monolayer $Nb_4C_3T_x$ MXene flake. The Cr/Au electrodes are colored in grayish yellow for clarity. e) I–V curves obtained from four-terminal measurements of the $Nb_4C_3T_x$ device shown in panel (d) at zero gate bias; see text for details. f) Two-terminal transfer characteristics of a monolayer $Nb_4C_3T_x$ FET. g) Temperature dependence of resistance of a monolayer $Nb_4C_3T_x$ device.

Figure 5e presents the results of the four-terminal measurements at zero gate bias for the device demonstrated in Figure 5d, showing the drain–source current (I_{DS}) as a function of drain–source bias (V_{DS}), as well as I_{DS} as a function of the voltage drop ($V_{12} = V_1 - V_2$) between the V_1 and V_2 electrodes recorded during the measurements. Both I_{DS}–V_{DS} and I_{DS}–V_{12} dependencies are linear, indicating the Ohmic behavior. The channel resistance measured

in the four-terminal configuration is $R_{ch} = 6.9$ kΩ, which taking the device dimensions into account corresponds to the sheet resistance of $R_s = 7.8$ kΩ $\square^{-1}$. Contact resistance, R_c, was estimated using the results of the I_{DS}–V_{DS} and I_{DS}–V_{12} measurements and the device dimensions. The calculated R_c of the device shown in Figure 5d at zero gate bias is about 170 Ω μm. Because of such low contact resistance, we considered the electrical characteristics obtained from two-terminal devices to be a good representation of the intrinsic properties of $Nb_4C_3T_x$ MXene flakes.

Table S1, Supporting Information, presents the results of electrical measurements of all studied devices. On average, the sheet resistance of monolayer $Nb_4C_3T_x$ MXene flakes is about 7.9 ± 1.1 kΩ $\square^{-1}$. Assuming the intrinsic thickness of an $Nb_4C_3T_x$ monolayer to be about 1.26 nm, the calculated resistivity of the material is 9.9 ± 1.4 μΩ m, corresponding to the electrical conductivity of 1024 ± 165 S cm^{-1}, which is two orders of magnitude higher than the values earlier reported for bulk $Nb_4C_3T_x$ assemblies.[20,23,33] The sheet resistance and the resistivity of 2L $Nb_4C_3T_x$ were found to be about 2.8 kΩ $\square^{-1}$ and 7.1 μΩ m (a conductivity of 1400 S cm^{-1}), respectively; for 3L $Nb_4C_3T_x$, the values are 1.5 kΩ $\square^{-1}$ and 5.5 μΩ m (a conductivity of 1800 S cm^{-1}), respectively. The resistivity of multilayer MXene flakes is slightly lower than for monolayers, which is likely because the inner layers in such flakes are protected from oxidation during the storage and device fabrication by the outer layers. This assumption is in agreement with the close values of electronic characteristics of 2L and 3L MXene flakes (Table S1, Supporting Information).

Figure 5f shows the I_{DS} dependence for an $Nb_4C_3T_x$ monolayer FET on the gate voltage (V_G) at room temperature and $V_{DS} = 0.1$ V. The drain current slightly increases with V_G, indicating that electrons are major charge carriers in $Nb_4C_3T_x$. From the transfer characteristics, we estimate the electron field-effect mobility (μ_{FE}) of 0.44 cm^2 V^{-1} s^{-1}, which is an order of magnitude lower than the electron mobility that we previously determined for $Ti_3C_2T_x$ MXene.[14] Other $Nb_4C_3T_x$ devices showed similar mobility values averaging at $\mu_{FE} = 0.41 ± 0.27$ cm^2 V^{-1} s^{-1} (Table S1, Supporting Information). The devices based on 2L and 3L $Nb_4C_3T_x$ flakes showed higher electron mobilities of about 0.7 cm^2 V^{-1} s^{-1} (Table S1, Supporting Information). This is consistent with the previous observations made for other solution-processable 2D materials, such as rGO flakes[34] and nanoribbons,[35] in which the electronic properties of devices noticeably improved when the thickness of the channel material increased from monolayer to bilayer, but did not show a comparable improvement with the

further increase in the number of layers. This is generally explained by the detrimental effects of a SiO_2 surface on the electronic transport in 2D monolayers, while in thicker flakes the bottom layers screen the upper layers from the substrate.[34,35]

The electrical properties of $Nb_4C_3T_x$ FETs were also tested at 77 K as presented in Figure S3 and Table S2, Supporting Information. Similar to the room temperature measurements, at 77 K, the devices also showed an Ohmic behavior. The average resistivity of the single-layer $Nb_4C_3T_x$ flakes at 77 K was 13.6 ± 2.9 $\mu\Omega$ m, which corresponds to the electrical conductivity of 610 ± 160 S cm^{-1}. The results of field-effect measurements (Figure S3, Supporting Information) showed no qualitative change in the character of electron transport upon cooling down to 77 K, and the mobility of the single-layer MXene flakes only slightly increased, averaging at 0.48 ± 0.26 cm^2 V^{-1} s^{-1} (Table S2, Supporting Information). This observation is consistent with the recent report on electrical measurements of another MXene material, Ti_3CNT_x, for which the mobility did not show a considerable variation with temperature either.[13] The room-temperature field-effect mobility measured for individual single-layer Ti_3CNT_x flakes was about 1.4 cm^2 V^{-1} s^{-1}, while the mobility extracted from the Hall effect measurements of a freestanding film of Ti_3CNT_x flakes was slightly lower (0.6 cm^2 V^{-1} s^{-1}) due to the effect of interflake contacts and remained nearly constant in the wide temperature range of 10–200 K.[13]

Figure 5g shows that the resistance of a single-layer $Nb_4C_3T_x$ MXene device slowly decreases with increasing temperature in the 77–300 K range. A similar resistance decrease was found for 2L and 3L MXene flakes as shown in Figure S4, Supporting Information, although the resistivity change was only about 20% compared to 40% for single-layer flakes (Table S2, Supporting Information). Qualitatively, similar temperature dependencies of resistance were also observed for some other MXenes.[13,36] The change of the resistance of MXene with temperature may depend not only on its intrinsic properties, but also on defects and surface terminations caused by the synthetic and processing conditions.[13]

5 Elastic Properties of Individual $Nb_4C_3T_x$ Single-Layer Flakes

For the mechanical measurements, we fabricated nanomembranes based on monolayer $Nb_4C_3T_x$ flakes and tested their elastic modulus and breaking strength by AFM nanoindentation. The detailed procedure for the fabrication of monolayer MXene membranes is described in our earlier work.[16] Briefly, a droplet of an aqueous suspension of

Nb$_4$C$_3$T$_x$ flakes was first placed on a freestanding PDMS support and dried in air. With a MXene side facing down, the PDMS support was placed on a Si/SiO$_2$ substrate with prefabricated microwells with diameters of 820 nm, and gently peeled off after a minute of contact, leaving some of the Nb$_4$C$_3$T$_x$ flakes on the silicon substrate. The sample was then examined with an optical microscope to locate microwells fully covered with monolayer Nb$_4$C$_3$T$_x$ flakes.

The described PDMS transfer method enables fabrication of well-stretched MXene membranes that are necessary for mechanical measurements.[16] This is illustrated by the AFM image in Figure 6a, which shows a representative monolayer Nb$_4$C$_3$T$_x$ membrane. The AFM height profile measured across the microwell shows that the membrane has a smooth surface and adheres to the walls of the well due to the attractive interaction between the hydrophilic MXene flake and SiO$_2$ (Figure 6b). The height profile also shows that the membrane is stretched at the height level of ≈17 nm below the surface of a flake on the substrate and therefore is well above the bottom of the microwell that is about 300 nm deep.
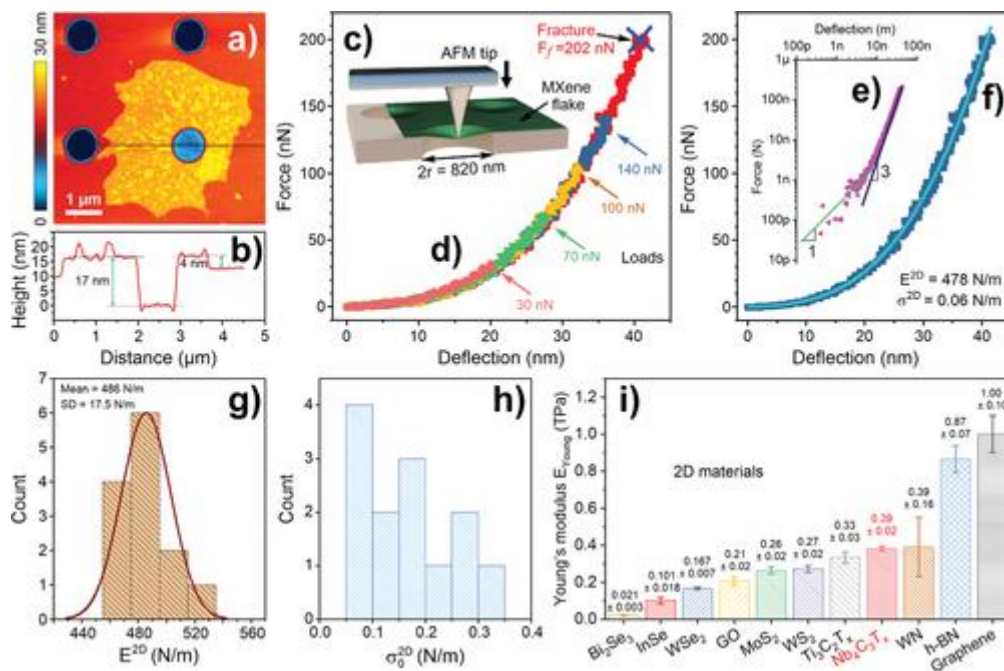

Figure 6. Characterization of mechanical properties of Nb$_4$C$_3$T$_x$ flakes. a) AFM image of an Nb$_4$C$_3$T$_x$ flake covering an 820 nm microwell in a Si/SiO$_2$ substrate. b) AFM height profile measured across the microwell along the dashed line in panel (a). c) Scheme of nanoindentation of a suspended Nb$_4$C$_3$T$_x$ membrane using an AFM tip. d) Force-deflection curves produced for a monolayer Nb$_4$C$_3$T$_x$ membrane at different loads. Fracture force is indicated by the blue cross. e) Loading curve for an Nb$_4$C$_3$T$_x$ MXene membrane in logarithmic coordinates. The curve

shows a linear behavior when the deflection does not exceed 10 nm (green line), and then a cubic dependence at high loads (blue line). f) Loading curve for a 1L $Nb_4C_3T_x$ membrane (squares) and the least squares fit (solid line) to the experimental data by Equation 1. g) Histogram of the elastic stiffness values for 1L $Nb_4C_3T_x$ membranes. Solid line represents a Gaussian fit to the data. h) Histogram of the prestress values for 1L $Nb_4C_3T_x$ membranes. i) Comparison of the effective Young's moduli of 1L $Nb_4C_3T_x$ and other 2D materials studied in similar nanoindentation experiments: multilayers of Bi_2Se_3,[37] InSe,[38] WSe_2,[39] and WN[40] and monolayers of GO,[41] MoS_2,[42,43] WS_2,[43] $Ti_3C_2T_x$,[16] h-BN,[44] and graphene.[45]

The scheme of the AFM nanoindentation experiment is presented in Figure 6c. A selected MXene flake was first imaged by AFM to locate the center of a membrane. Then, we used a diamond-coated AFM tip to perform nanoindentation on the membrane's center while recording the applied force (F) and the deflection of a membrane (δ). When a predefined force was reached, the tip was pulled up and the membrane was imaged by AFM again to confirm that the flake was not deformed. The F–δ curves were recorded for both forward and backward AFM tip loads; the representative data are shown in Figure S5, Supporting Information. The same membrane was tested several times increasing the load with every consecutive measurement, as shown in Figure 6d. Both forward and backward F–δ curves as well as the F–δ curves for subsequent loads coincided, which confirms that the membrane deformed elastically, and no flake sliding occurred. Finally, at some force, the membrane fractured; this maximum F_f is indicated by the blue cross in Figure 6d.

The recorded F–δ curves were then processed to extract the mechanical characteristics of $Nb_4C_3T_x$ membranes. Assuming isotropic character of $Nb_4C_3T_x$, the AFM tip, and the microwells, we can fit the experimental F–δ data using the formula

$$F = \sigma_0^{2D}\pi\delta + E^{2D}\frac{q^3\delta^3}{r^2} \qquad (1)$$

where σ^{2D}_0 represents prestress in the membrane, E^{2D} is the 2D elastic modulus, and r is the radius of the well.[42,45] The dimensionless constant q is related to v, the Poisson's ratio (0.227 for NbC[21]), as $q = 1/(1.049 - 0.15v - 0.16v^2) = 0.9933$. Equation 1 consists of linear and cubic terms. Figure 6e shows the F–δ dependence for an $Nb_4C_3T_x$ membrane in logarithmic coordinates, where these two terms are visualized. At small loads (less than 10 nN), the dependence is linear as indicated by the green solid line and corresponds to the prestretched membrane regime. At the loads larger than 10 nN, the membrane demonstrates nonlinear

behavior and is characterized by a cubic $F \approx \delta^3$ relationship (blue solid line) from which E^{2D} can be extracted. Figure 6f shows the experimental and fitting curves for a monolayer $Nb_4C_3T_x$ flake with the goodness of fit $R^2 = 0.996$.

We studied the mechanical properties of two $Nb_4C_3T_x$ membranes from different flakes. Each membrane was measured several times at different loads, totaling 13 experimental $F–\delta$ curves. The analysis of experimental data using Equation 1 revealed a quite narrow distribution of the E^{2D} parameter, which ranged from 462 to 511 N m^{-1}, as shown in Figure 6g. Based on 13 measurements, the average value of the elastic modulus E^{2D} is 486 ± 18 N m^{-1}. The prestress σ^{2D}_0 ranged from 0.06 to 0.32 N m^{-1} for monolayer $Nb_4C_3T_x$ flakes; the corresponding histogram of the prestress values is shown in Figure 6h. The $\sigma2D0\sigma02D$ is comparable with the values obtained for graphene,[45] MoS$_2$,[42] and $Ti_3C_2T_x$ membranes,[16] and shows a strong interaction between $Nb_4C_3T_x$ MXene membranes and the walls of microwells. Finally, both $Nb_4C_3T_x$ MXene flakes fractured at almost the same maximum loads F_f of 202 and 206 nN. We can extract the maximum stress σ^{2D}_{max} using the expression for the indentation of a linearly elastic circular membrane under a spherical indenter[46]

$$\sigma^{2D}_{max} = \sqrt{\frac{F_f E^{2D}}{4\pi r_{tip}}} \quad (2)$$

For the AFM diamond tip radius (r_{tip}) of 7 nm used in this work, $\sigma^{2D}_{max} = 33$ N m^{-1}. This value is about 6.8% of the Young's modulus E^{2D} for monolayer $Nb_4C_3T_x$, which is slightly higher than what we observed for $Ti_3C_2T_x$ at 5.2%,[16] but still lower than the theoretical upper limit of a material's breaking strength.[47] The latter is probably due to the presence of structural defects in the material, which is also indicated by the non-catastrophic fracture of $Nb_4C_3T_x$ membranes as observed in the AFM image of a locally punctured flake in Figure S6, Supporting Information.[48]

The effective Young's modulus E_{Young} and breaking strength σ_{max}, which allow comparison with other 2D materials, can be calculated by dividing E^{2D} and σ^{2D}_{max} by the membrane's thickness of 1.26 nm. The effective Young's modulus for $Nb_4C_3T_x$ monolayers was calculated to be 386 ± 13 GPa and the breaking strength was determined to be 26 ± 1.6 GPa. A comparison of the E_{Young} values for $Nb_4C_3T_x$ and other benchmark 2D materials is presented in Figure 6i. The effective Young's modulus of $Nb_4C_3T_x$ exceeds the reported values for CVD-grown or mechanically exfoliated Bi_2Se_3,[37] InSe,[38] WSe$_2$,[39] MoS$_2$,[42,43] and WS$_2$,[43] is comparable to E_{Young} of the recently reported CVD-grown multilayer WN crystals,[40] but is lower than the

Young's moduli of perfect monolayers of mechanically exfoliated graphene[45] and h-BN.[44] However, it is more imperative to compare the mechanical properties of $Nb_4C_3T_x$ to other solution-processable 2D materials, such as GO, rGO, and $Ti_3C_2T_x$, the most extensively studied MXene. As both GO/rGO and MXenes can be synthesized in bulk quantities as easily processable dispersions of 2D sheets, they are often discussed with respect to similar applications, such as conductive coatings and polymer composites, for many of which the mechanical characteristics of the sheets are very important. Previously, we demonstrated that based on the results of similar nanoindentation measurements, $Ti_3C_2T_x$ MXene has a higher effective Young's modulus of about 330 GPa[16] than ≈210 GPa reported for GO.[41] As this work shows, another MXene material, $Nb_4C_3T_x$, offers an even higher effective Young's modulus of 386 ± 13 GPa, establishing a new record for solution-processable 2D materials (Figure 6i).

The Young's modulus of $Nb_4C_3T_x$ monolayer was measured to be slightly smaller than that of cubic NbC (452–488 GPa),[21,22] which could be related to the presence of structural defects introduced during the acid etching of the precursor MAX phase, as well as the T_x functionalities that increase the nominal thickness of MXene sheets while not bolstering their mechanical properties. Yet, the closeness of the Young's moduli obtained for cubic NbC and $Nb_4C_3T_x$ monolayers suggests that the mechanical properties of bulk carbide materials could serve as reasonable estimates for assessing the mechanical properties of related MXenes (Figure 1). Also, the results of the AFM nanoindentation measurements on monolayer membranes of $Ti_3C_2T_x$[16] and $Nb_4C_3T_x$ (this work) generally agree with our initial comparative assessment of their Young's moduli based on the known mechanical properties of cubic TiC[19] and NbC.[21,22] Thus, the available information on other known bulk carbides could be useful for identifying MXene materials with even better mechanical properties and inspire chemists to synthesize such materials in cases when the corresponding MXene compositions have not been yet experimentally realized.

6 Conclusion

In summary, we report an improved synthesis of $Nb_4C_3T_x$ MXene which yields large (up to 20 µm in size) high-quality individual flakes suitable for mechanical and electrical measurements. Characterization of the electrical properties of $Nb_4C_3T_x$ monolayers showed a conductivity of 1024 ± 165 S cm^{-1}, which is a two orders of magnitude improvement compared to the previously reported values for bulk $Nb_4C_3T_x$ assemblies.[20] This result demonstrates the

importance of single-flake measurements for revealing the intrinsic physical properties of MXene materials. $Nb_4C_3T_x$ devices with Cr/Au contacts exhibit Ohmic behavior with a low contact resistance of 170 Ω μm and field-effect electron mobilities $\mu_{FE} = 0.41 \pm 0.27$ cm^2 V^{-1} s^{-1}. We also tested the mechanical properties of monolayer $Nb_4C_3T_x$ membranes by AFM nanoindentation and found the effective Young's modulus $E_{Young} = 386 \pm 13$ GPa and the breaking strength $\sigma_{max} = 26 \pm 1.6$ GPa. The former is the highest value reported for nanoindentation measurements of solution-processable 2D materials, such as GO, rGO and $Ti_3C_2T_x$ MXene, revealing the potential of $Nb_4C_3T_x$ as a primary component of structural composites, protective coatings, membranes, textiles, and other applications. Finally, we discuss the agreement between the mechanical properties of 2D $Nb_4C_3T_x$ MXene and 3D cubic NbC, and suggest that the extensive experimental data on bulk carbides could be useful for identifying new MXene materials with improved functional characteristics and inspire chemists and materials scientists to their synthesis and characterization.

7 Experimental Section

Scanning Electron Microscopy

SEM analysis was performed using a Zeiss Supra 40 field-emission scanning electron microscope at the accelerating voltage of 5 kV.

XRD patterns were recorded using a Rigaku SmartLab powder diffractometer with Ni-filtered Cu Kα radiation operated at 40 kV and 15 mA. The 0.03° step and 0.5 s dwelling time were used to collect the XRD patterns.

Transmission Electron Microscopy

$Nb_4C_3T_x$ flakes were visualized using a FEI Tecnai Osiris scanning transmission electron microscope equipped with a high-angle annular dark-field detector and X-FEG high brightness Schottky field emission gun. The accelerating voltage was 200 kV.

X-Ray Photoelectron Spectroscopy

XPS was performed using a Thermo Scientific K-Alpha X-ray photoelectron spectrometer with a monochromatic Al Kα (1486.6 eV) X-ray source. The XPS Nb$3d$ spectrum was recorded at room temperature with a step of 0.1 eV using a pass energy of 20 eV and a low kinetic energy electron flood gun.

UV−vis−NIR absorption spectra were recorded using a Jasco V-670 spectrophotometer.

Device Fabrication

A Zeiss Supra 40 field-emission scanning electron microscope and a Raith Pattern Generator were used for electron beam lithography to pattern electrodes on $Nb_4C_3T_x$ flakes. An AJA electron beam evaporation system at the base pressure of $\approx 8 \times 10^{-9}$ Torr was used to evaporate 5 nm of Cr at 0.1 Å s^{-1} rate and 20 nm of Au at 0.2 Å s^{-1} rate.

Electrical Measurements

The $Nb_4C_3T_x$ devices were measured in a Lake Shore TTPX cryogenic probe station at a base pressure of about 2×10^{-6} Torr. The electrical measurements were performed using an Agilent 4155C semiconductor parameter analyzer that was linked to a computer through 82357B USB/GPIB interface and controlled using a National Instruments LabVIEW code. The temperature was modulated using liquid nitrogen as a cryogenic liquid and a Lake Shore 336 temperature controller.

Atomic Force Microscopy

AFM of $Nb_4C_3T_x$ devices was performed using a Digital Instruments Nanoscope IIIa Dimension 3100 scanning probe microscope.

Nanoindentation Experiments

Surface topography imaging and force-indentation curve measurements of $Nb_4C_3T_x$ membranes were performed on an Asylum Research MFP-3D system. Single crystal diamond tips (D80, SCD probes) with tip radius of 5–10 nm and spring constant ≈ 3.5 N m^{-1}, according to the manufacturer's specifications, were used for force-indentation experiments. The spring constant of each AFM cantilever was calibrated via thermal noise method before indentation experiments. During the force-indentation experiments, the z-piezo displacement speed was controlled at 100 nm s^{-1} rate. Different rates ranging from 50 to 1000 nm s^{-1} were also tested and showed no clear difference for the force-indentation curves.

Analysis of Force-Indentation Curves

During the indentation experiments, the cantilever bending and z-piezo displacement were recorded as the tip moved downward. The cantilever bending was calibrated by first measuring

a force-displacement curve on a hard Si/SiO$_2$ surface. The loading force was obtained by multiplying the cantilever bending by the cantilever spring constant, and the deflection of the membrane was obtained by subtracting the cantilever bending from the z-piezo displacement. In the experimental force-deflection data, there is a negative force section due to the tip jump-to-surface effect, where the tip snaps down to the membrane attracted by van der Waals forces when it is very close to the surface.[16] We extrapolated the zero force line in the force-deflection dependence prior to snapping until it crossed the curve. This point, in which the force and displacement are both zero, was considered as a center of origin in the following analysis of the force-deflection relationship. A more detailed discussion of the analysis of force-indentation curves for MXene membranes is provided in our previous work.[16]

Acknowledgements

Conflict of Interest

The authors declare no conflict of interest.

References

[1] F. Shahzad, M. Alhabeb, C. B. Hatter, B. Anasori, S. Man Hong, C. M. Koo, Y. Gogotsi, Science 2016, 353, 1137.

[2] S. J. Kim, H.-J. Koh, C. E. Ren, O. Kwon, K. Maleski, S.-Y. Cho, B. Anasori, C.-K. Kim, Y.-K. Choi, J. Kim, Y. Gogotsi, H.-T. Jung, ACS Nano 2018, 12, 986.

[3] A. Sarycheva, A. Polemi, Y. Liu, K. Dandekar, B. Anasori, Y. Gogotsi, Sci. Adv. 2018, 4, eaau0920.

[4] R. Li, W. Sun, C. Zhan, P. R. C. Kent, D.-E. Jiang, Phys. Rev. B 2019, 99, 085429.

[5] M. R. Lukatskaya, O. Mashtalir, C. E. Ren, Y. Dall'Agnese, P. Rozier, P. L. Taberna, M. Naguib, P. Simon, M. W. Barsoum, Y. Gogotsi, Science 2013, 341, 1502.

[6] B. Anasori, M. R. Lukatskaya, Y. Gogotsi, Nat. Rev. Mater. 2017, 2, 16098.

[7] F. Meng, M. Seredych, C. Chen, V. Gura, S. Mikhalovsky, S. Sandeman, G. Ingavle, T. Ozulumba, L. Miao, B. Anasori, Y. Gogotsi, ACS Nano 2018, 12, 10518.

[8] K. Huang, Z. Li, J. Lin, G. Han, P. Huang, Chem. Soc. Rev. 2018, 47, 5109.

[9] H. Lin, Y. Wang, S. Gao, Y. Chen, J. Shi, Adv. Mater. 2018, 30, 1703284.

[10] M. Naguib, Y. Gogotsi, Acc. Chem. Res. 2015, 48, 128.

[11] M. Ghidiu, M. R. Lukatskaya, M.-Q. Zhao, Y. Gogotsi, M. W. Barsoum, Nature 2014, 516, 78.

[12] B. Anasori, Y. Gogotsi, 2D Metal Carbides and Nitrides (MXenes): Structure, Properties and Applications, Springer, Cham, Switzerland 2019.

[13] K. Hantanasirisakul, M. Alhabeb, A. Lipatov, K. Maleski, B. Anasori, P. Salles, C. Ieosakulrat, P. Pakawatpanurut, A. Sinitskii, S. J. May, Y. Gogotsi, Chem. Mater. 2019, 31, 2941.

[14] A. Lipatov, M. Alhabeb, M. R. Lukatskaya, A. Boson, Y. Gogotsi, A. Sinitskii, Adv. Electron. Mater. 2016, 2, 1600255.

[15] A. Miranda, J. Halim, M. W. Barsoum, A. Lorke, Appl. Phys. Lett. 2016, 108, 033102.

[16] A. Lipatov, H. Lu, M. Alhabeb, B. Anasori, A. Gruverman, Y. Gogotsi, A. Sinitskii, Sci. Adv. 2018, 4, eaat0491.

[17] M. Alhabeb, K. Maleski, B. Anasori, P. Lelyukh, L. Clark, S. Sin, Y. Gogotsi, Chem. Mater. 2017, 29, 7633.

[18] Y. Gogotsi, R. A. Andrievski, Materials Science of Carbides, Nitrides and Borides, Kluwer, Dordrecht, The Netherlands 1999.

[19] R. Chang, L. J. Graham, J. Appl. Phys. 1966, 37, 3778.

[20] M. Ghidiu, M. Naguib, C. Shi, O. Mashtalir, L. M. Pan, B. Zhang, J. Yang, Y. Gogotsi, S. J. L. Billinge, M. W. Barsoum, Chem. Commun. 2014, 50, 9517.

[21] R. F. Brenton, C. R. Saunders, C. P. Kempter, J. Less-Common Met. 1969, 19, 273.

[22] H. L. Brown, P. E. Armstrong, C. P. Kempter, J. Chem. Phys. 1966, 45, 547.

[23] S. Zhao, X. Meng, K. Zhu, F. Du, G. Chen, Y. Wei, Y. Gogotsi, Y. Gao, Energy Storage Mater. 2017, 8, 42.

[24] A. Buchsteiner, A. Lerf, J. Pieper, J. Phys. Chem. B 2006, 110, 22328.

[25] X. Wang, X. Shen, Y. Gao, Z. Wang, R. Yu, L. Chen, J. Am. Chem. Soc. 2015, 137, 2715.

[26] M. Naguib, J. Halim, J. Lu, K. M. Cook, L. Hultman, Y. Gogotsi, M. W. Barsoum, J. Am. Chem. Soc. 2013, 135, 15966.

[27] H. Lin, S. Gao, C. Dai, Y. Chen, J. Shi, J. Am. Chem. Soc. 2017, 139, 16235.

[28] J. C. Shearer, D. A. Slattery, J. A. Stapleton, G. J. Shapter, T. C. Gibson, Nanotechnology 2016, 27, 125704.

[29] K. S. Novoselov, D. Jiang, F. Schedin, T. J. Booth, V. V. Khotkevich, S. V. Morozov, A. K. Geim, Proc. Natl. Acad. Sci. USA 2005, 102, 10451.

[30] J. S. Cameron, D. S. Ashley, J. S. Andrew, G. S. Joseph, T. G. Christopher, Nanotechnology 2016, 27, 125704.

[31] C. E. Giusca, V. Panchal, M. Munz, V. D. Wheeler, L. O. Nyakiti, R. L. Myers-Ward, D. K. Gaskill, O. Kazakova, Adv. Mater. Interfaces 2015, 2, 1500252.

[32] H. Lu, B. Wang, T. Li, A. Lipatov, H. Lee, A. Rajapitamahuni, R. Xu, X. Hong, S. Farokhipoor, L. W. Martin, C.-B. Eom, L.-Q. Chen, A. Sinitskii, A. Gruverman, Nano Lett. 2016, 16, 6460.

[33] C. Zhang, S. J. Kim, M. Ghidiu, M.-Q. Zhao, M. W. Barsoum, V. Nicolosi, Y. Gogotsi, Adv. Funct. Mater. 2016, 26, 4143.

[34] C. Gómez-Navarro, R. T. Weitz, A. M. Bittner, M. Scolari, A. Mews, M. Burghard, K. Kern, Nano Lett. 2007, 7, 3499.

[35] A. Sinitskii, A. Dimiev, D. V. Kosynkin, J. M. Tour, ACS Nano 2010, 4, 5405.

[36] B. Anasori, C. Shi, E. J. Moon, Y. Xie, C. A. Voigt, P. R. C. Kent, S. J. May, S. J. L. Billinge, M. W. Barsoum, Y. Gogotsi, Nanoscale Horiz. 2016, 1, 227.

[37] H. Yan, C. Vajner, M. Kuhlman, L. Guo, L. Li, P. T. Araujo, H.-T. Wang, Appl. Phys. Lett. 2016, 109, 032103.

[38] Y. Li, C. Yu, Y. Gan, Y. Kong, P. Jiang, D.-F. Zou, P. Li, X.-F. Yu, R. Wu, H. Zhao, C.-F. Gao, J. Li, Nanotechnology 2019, 30, 335703.

[39] R. Zhang, V. Koutsos, R. Cheung, Appl. Phys. Lett. 2016, 108, 042104.

[40] H. Wang, E. J. Sandoz-Rosado, S. H. Tsang, J. Lin, M. Zhu, G. Mallick, Z. Liu, E. H. T. Teo, Adv. Funct. Mater. 2019, 29, 1902663.

[41] J. W. Suk, R. D. Piner, J. An, R. S. Ruoff, ACS Nano 2010, 4, 6557.

[42] S. Bertolazzi, J. Brivio, A. Kis, ACS Nano 2011, 5, 9703.

[43] K. Liu, Q. M. Yan, M. Chen, W. Fan, Y. H. Sun, J. Suh, D. Y. Fu, S. Lee, J. Zhou, S. Tongay, J. Ji, J. B. Neaton, J. Q. Wu, Nano Lett. 2014, 14, 5097.

[44] A. Falin, Q. Cai, E. J. G. Santos, D. Scullion, D. Qian, R. Zhang, Z. Yang, S. Huang, K. Watanabe, T. Taniguchi, M. R. Barnett, Y. Chen, R. S. Ruoff, L. H. Li, Nat. Commun. 2017, 8, 15815.

[45] C. Lee, X. Wei, J. W. Kysar, J. Hone, Science 2008, 321, 385. [46] N. M. Bhatia, W. Nachbar, Int. J. Non-Linear Mech. 1968, 3, 307.

[47] X. Sang, Y. Xie, M.-W. Lin, M. Alhabeb, K. L. Van Aken, Y. Gogotsi, P. R. C. Kent, K. Xiao, R. R. Unocic, ACS Nano 2016, 10, 9193.

[48] G. López-Polín, J. Gómez-Herrero, C. Gómez-Navarro, Nano Lett. 2015, 15, 2050.